

Article

A Visible-Light-Active CuS/MoS₂/Bi₂WO₆ Aptamer Sensitive Detects the Non-Steroidal Anti-Inflammatory Drug Diclofenac

Yun He, Hongjie Gao and Jiankang Liu *

The Key Laboratory of Biomedical Information Engineering of Ministry of Education, School of Life Science and Technology, Xi'an Jiaotong University, Xi'an 710049, China

* Correspondence: liujiankang2021@hotmail.com

Abstract: Diclofenac is a non-steroidal, anti-inflammatory drug and is clinically used for the treatment of osteoarthritis, non-articular rheumatism, etc. This research aimed to demonstrate the creation of an upgraded photoelectrochemical (PEC) aptamer sensor for detecting diclofenac (DCF) with high sensitivity. In this work, photoactive materials and bio-identification components served as visible-light-active CuS/MoS₂/Bi₂WO₆ heterostructures and aptamers, respectively. CuS and MoS₂/Bi₂WO₆ were combined to improve photocurrent responsiveness, which helped the structure of PEC aptasensors. Additionally, the one-pot synthesis of CuS/MoS₂/Bi₂WO₆ was ecologically beneficial. With these optimizations, the photocurrent response of aptamer/CS/CuS/MoS₂/Bi₂WO₆ exhibited linearity between 0.1 and 500 nM DCF. The detection limit was 0.03 nM (S/N = 3). These results suggest that the PEC sensing technique might produce an ultra-sensitive sensor with high selectivity and stability for DCF detection.

Keywords: photoelectrochemical; CuS/MoS₂/Bi₂WO₆; diclofenac (DCF); heterostructure; aptasensors



Citation: He, Y.; Gao, H.; Liu, J. A Visible-Light-Active CuS/MoS₂/Bi₂WO₆ Aptamer Sensitive Detects the Non-Steroidal Anti-Inflammatory Drug Diclofenac. *Nanomaterials* **2022**, *12*, 2834. <https://doi.org/10.3390/nano12162834>

Academic Editors: Deepak Kukkar and Ki-Hyun Kim

Received: 27 June 2022

Accepted: 8 August 2022

Published: 18 August 2022

Publisher's Note: MDPI stays neutral with regard to jurisdictional claims in published maps and institutional affiliations.



Copyright: © 2022 by the authors. Licensee MDPI, Basel, Switzerland. This article is an open access article distributed under the terms and conditions of the Creative Commons Attribution (CC BY) license (<https://creativecommons.org/licenses/by/4.0/>).

1. Introduction

Diclofenac (DCF) is a non-steroidal, anti-inflammatory drug (NSAID) marketed for global consumption [1]. It has been utilized for surgical procedures such as gynecological, orthopedic, and ontological procedures [2]. Additionally, DCF specializes in the treatment of osteoarthritis, renal and biliary cramps, pharyngotonsillitis, otitis, annexites, and primary dysmenorrhea, as well as various infection-related pain operations [1–3]. According to a study in 2018, around half of the original medication was metabolized; moreover, 70% of pharmaceuticals was excreted via urine, despite diverse conditions occurring in relation to those targeted drugs [4]. The risk assessment of drug toxicity revealed that, according to data on the DCF presence in wastewater following standard biological treatment, around 80% of the original pollutant was retained [5]. Inefficient effluent treatment plants that failed to eliminate drugs from wastewater were utilized to develop four drug detection techniques.

Many methods have been employed for DCF detection, such as immunoassays, chromatographic techniques, and electrochemical methods [6–8]. Clearly, these techniques, which provide the efficient detection of DCF at concentrations ranging from M to nM, are not without limitations, including the requirement for costly equipment. Additionally, they consume significantly more time and need complicated preprocessing, limiting their practical applicability [9,10]. As a result, a sensitive and selective sensor capable of providing more promptness and ease for DCF detection needs to be built.

Photoelectrochemical (PEC) sensors, which specialize in high sensitivity, simply structured instruments, easily conducted downsizing, and low prices, have previously attracted academics to conduct research on them [11–13]. When developing PEC sensors, improved photocatalyst performance contributes to increased sensitivity. Nonetheless, PEC sensing must rely on photocatalytic processes that lack analyte specificity. To overcome the issue, significant efforts have been made to improve the selectivity of PEC sensors by including

numerous recognition components such as molecular-imprinted polymers, enzymes, antibodies, and aptamers [14,15]. In terms of these factors, aptamers, well-known antibody mimetics with excellent recognition capacity over particular targets, have been used to build highly selective PEC aptasensors orientated with a more extensive variety of analytes consisting of inorganic ions, proteins, cells, antibiotics, and chemical substances.

Some bismuth-based semiconductors also have a hybrid orbital of Bi 6s and O 2p, decreasing the bandgap while generating a deep valance band, such as BiOI, Bi₂S₃, Bi₂XO₆ (X = Mo, W), and others [16,17]. These elements, characterized by abundance, low toxicity, and low cost, have become the target of intense studies in PEC research [18]. Furthermore, the morphological structure of Bi₂WO₆, which includes Bi₂O₂ layers and WO₆ octahedral structure layers, has a significant impact on its physical and chemical characteristics [19]. Furthermore, Bi₂WO₆ is one of the possible visible-light-driven photocatalysts with a moderate band gap (approximately 2.5 eV) [20]. More Bi₂WO₆ uses emerged in recent years, including PEC solar cells, PEC sensors, and photoelectrocatalytic hydrogen generation [21–23]. However, high-degree recombination specialized in photoexcited carriers, comparably weak light consumption capacity in pure Bi₂WO₆, and specialized poor photocatalytic activity severely restricted the highlighted practical uses in the environment [24]. As a result, significant efforts have been undertaken to address these shortcomings. Semiconductor coupling and metal particle deposition coupling with carbon materials are two examples [23,24].

MoS₂ exhibits a photocatalytic capability due to its differentially specialized structure of sandwich layers of S–Mo–S atoms [25]. Furthermore, according to the current study, MoS₂ has better photocatalytic activity because to its differentiated electrical and optical characteristics and large surface area [26]. As a result, MoS₂ was used in numerous materials, including BiVO₄ [18], WS₂ [26], and TiO₂ [27], to increase electron–hole pair separation and PEC performance. Semiconductor chalcogenides have attracted tremendous attention with high abundance and low cost. Copper sulfide (CuS), which performs the duty of p-type semiconductors, presents availability, versatility, low toxicity, etc. [28]. Moreover, it also has unique electronic and optical properties, with additional applications to catalysis, solar cell, sensing, and lithium-ion batteries. CuS, a narrow-band gap semiconducting material (approximately 1.7 eV), is employed for coupling with bismuth-based semiconductors for enhanced photocatalytic performance [29,30].

Based on the abovementioned background research, a CuS/MoS₂/Bi₂WO₆ photoactive material was developed. By demonstrating greater photocurrents, CuS/MoS₂/Bi₂WO₆ extended the light response to the visible region beyond the elements of Bi₂WO₆ and MoS₂/Bi₂WO₆ alone. As a result of the increased photo-to-current efficiency, it was proven that Bi₂WO₆ sensitized with CuS and MoS₂ may promote photogenerated electron-hole pair separation. The improved CuS/MoS₂/Bi₂WO₆ photoactive material enabled the unification of a large linear range with a low detection limit, resulting in a successful PEC aptasensor for DCF detection. This novel PEC sensing strategy provides a highly selective and robust detection method for DCF detection. Moreover, the sensor also has good application prospects in practical applications. This also demonstrates the enormous potential of CuS/MoS₂/Bi₂WO₆ nanocomposites in fields such as PEC sensing, photocatalysis, and others.

2. Experimental Section

2.1. Materials and Reagents

Thiourea (SC(NH₂)₂), ethanol (99.7%), bismuth nitrate pentahydrate (Bi(NO₃)₃·5H₂O), copper nitrate trihydrate (Cu(NO₃)₂·3H₂O), sodium tungstate dihydrate (Na₂WO₄·5H₂O), glacial acetic acid (99.7%), glutaraldehyde (GA, 50%), and tris (hydroxymethyl) aminomethane (Tris) were purchased from Sinopharm (Shanghai, China). Chitosan (CS, 95%) was obtained from Sigma-Aldrich (America). DCF sodium drugs were obtained from Aladdin (Beijing, China). All other reagents were of analytical reagent grade. The amino-functionalized DCF aptamer (5'-NH₂-TCTA ACGT GAAT GATA GACC TGCC TTGG GTGG TGGG

CGAC TGAC TGGC GGTG CAAC GTTA ACTT ATTC GACC ATA-3') was composed by the Shanghai Sangon Biotech Co., Ltd. (Shanghai, China) and purified via an HPLC technique. The aptamer solution was compounded by dissolving aptamer into the Tris-HCl buffer (0.1 M, pH 7.4). Phosphate-buffered solution (PBS, 0.1 M, pH 7.4) was prepared from Na_2HPO_4 and NaH_2PO_4 and exploited as an electrolyte during the period of detection, while double-distilled water (Milli-Q, Millipore) was used for all aqueous solutions throughout the experiment. The rpm of the washing steps was 8000 r/min.

2.2. Preparations of All Materials

Bi_2WO_6 material synthesis: 2 mmol of $\text{Bi}(\text{NO}_3)_3 \cdot 5\text{H}_2\text{O}$ (0.9702 g) was added to ultrapure water (40 mL). Then, 1 mmol of $\text{Na}_2\text{WO}_4 \cdot 5\text{H}_2\text{O}$ (0.3838 g) was added to obtain the suspension slowly and appropriately under continuous stirring. Subsequently, the mixed suspension received another 1 h of stirring. After being transferred to a Teflon-lined autoclave (100 mL), the mixed solution underwent 20 h of heating treatment at 180 °C. At last, deionized water together with ethanol helped to wash the product three times, followed by drying treatment at 60 °C.

$\text{MoS}_2/\text{Bi}_2\text{WO}_6$ composite synthesis: 1 mmol of Bi_2WO_6 was added to 20 mL of ultrapure water, and different contents of $(\text{NH}_4)_6\text{Mo}_7\text{O}_{24} \cdot 4\text{H}_2\text{O}$ (0.1412 mg, 3.531 mg, and 5.2965 mg) and $\text{SC}(\text{NH}_2)_2$ (0.1218 mg, 0.3044 mg, and 0.4568 mg) were added to the suspension obtained above with continuous stirring. After being transferred to a 50 mL Teflon-lined autoclave, the mixed solution underwent 24 h of heating at 200 °C. The obtained samples were washed and calcined. The material was named $\text{MoS}_2/\text{Bi}_2\text{WO}_6$ -2%, $\text{MoS}_2/\text{Bi}_2\text{WO}_6$ -5%, and $\text{MoS}_2/\text{Bi}_2\text{WO}_6$ -7% (2%, 5%, and 7% = $m(\text{MoS}_2)/[m(\text{MoS}_2) + m(\text{Bi}_2\text{WO}_6)]$).

$\text{CuS}/\text{MoS}_2/\text{Bi}_2\text{WO}_6$ composite synthesis: 1 mmol of $\text{MoS}_2/\text{Bi}_2\text{WO}_6$ (0.6711 g) was added to 20 mL of ultrapure water, and different contents of $\text{SC}(\text{NH}_2)_2$ (4.5672 mg) and $\text{Cu}(\text{NO}_3)_2 \cdot 3\text{H}_2\text{O}$ (14.496 mg) were added to the suspension obtained above, which were stirred continuously. Subsequently, the mixed suspension received another 30 min of stirring, and then, 10 mL of ethanol solution was added. After being transferred to a 50 mL Teflon-lined autoclave, the mixed solution underwent 12 h of heating at 200 °C.

2.3. Characterization

A Bruker D8 Advance diffractometer (Billerica, MA, USA) equipped with $\text{Cu K}\alpha$ radiation was applied to perform the X-ray diffraction (XRD) ($\lambda = 0.154056$ nm). An ESCALAB 250Xi (Thermo Fisher Scientific, Waltham, MA, USA) was employed to carry out the X-ray photoelectron spectroscopy (XPS). A UV-visible (UV-vis) spectrophotometer was employed to collect the diffuse reflection spectra (DRS) exhibited by these materials with BaSO_4 as the background between 200 and 800 nm. Scanning electron microscopy (SEM) together with transmission electron microscopy (TEM, at 200 kV) were used to characterize the morphology exhibited by these samples.

2.4. Construction of PEC Aptasensor

Indium tin oxide (ITO, 1 cm × 2 cm) electrodes were ultrasonically cleaned sequentially in NaOH solution (0.1 M), ethanol, and ultrapure water. They were then dried under infrared light. The PEC aptasensor was prepared using the following steps. Firstly, 20 μL of $\text{CuS}/\text{MoS}_2/\text{Bi}_2\text{WO}_6$ suspension (6 g/L, 500 mL) was modified onto ITO within a fixed geometric region (0.5 cm × 1 cm) and dried under room temperature to form a $\text{CuS}/\text{MoS}_2/\text{Bi}_2\text{WO}_6$ electrode. Then, 20 μL of CS (0.05%), acting as fixing agent, was dropped onto the $\text{CuS}/\text{MoS}_2/\text{Bi}_2\text{WO}_6$ and dried off at room temperature. Next, 10 μL of 2.5% GA aqueous solution (a cross linker for the amino functional aptamer) was put onto the above electrode and kept for 1 h at 25 °C, followed by rinsing with PBS (0.1 M, pH 7.4) to eliminate excess GA. The resultant surface was coated with 10 μL of amine-functionalized aptamer solution (1 μM) and incubated at 4 °C for 12 h. The prepared sensor of aptamer/CS/ $\text{CuS}/\text{MoS}_2/\text{Bi}_2\text{WO}_6$ was washed with PBS to eliminate any unbounded aptamer. It should be highlighted that the NH_2 group in the DCF aptamer was covalently

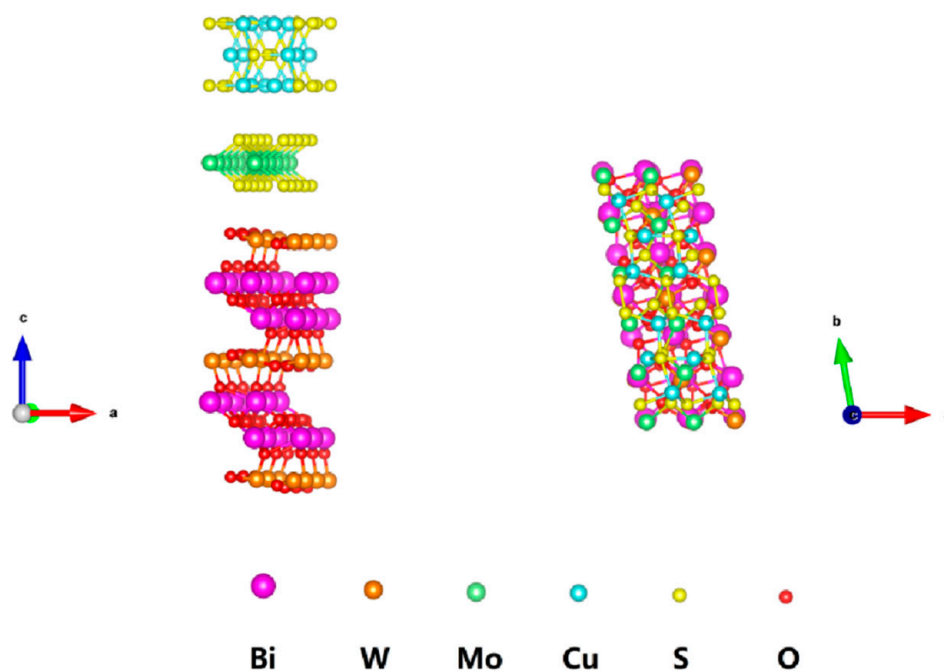
attached to the NH_2 group of the immobilized CS on the ITO surface, using GA as the linking agent. Ultimately, the PEC aptasensors were obtained.

2.5. Electrochemical Experiments

The measurements of the PEC were made with a CHI 660E electrochemical workstation (CH Instrument Company, Shanghai, China). A conventional three-electrode system cell was employed. Pt wire was used as the counter electrode, a saturated calomel electrode (SCE) was the reference electrode, and ITO glass was the working electrode. The light source came from a xenon lamp (PLS-SXE 300, 100 mW cm^{-2} , $\lambda \geq 420 \text{ nm}$), and the light source was kept at 15 cm while the modified electrode was applied in the PEC system to detect DCF at an operating potential of 0.1 V. Electrochemical impedance spectroscopy (EIS) was performed in PBS (0.1 M, pH = 7). To investigate the detection performance of the PEC aptasensor, the prepared aptamer/CS/CuS/MoS₂/Bi₂WO₆ electrode was incubated with 20 μL of DCF solution at various concentrations for 40 min.

2.6. Computational Methodology

First-principle calculations were carried out using density functional theory (DFT) with generalized gradient approximation (GGA) of Perdew–Burke–Ernzerhof (PBE) implemented in the Vienna Ab-Initio Simulation Package (VASP) (Scheme 1). The valence electronic states were expanded on the basis of plane waves with the core–valence interaction represented using the projector augmented plane wave (PAW) approach and a cutoff of 520 eV. A Γ -centered k-mesh of $3 \times 3 \times 1$ points was used for the calculations. Convergence was achieved when the forces acting on ions became smaller than $0.02 \text{ eV}/\text{\AA}$.



Scheme 1. DFT-optimized composite structure.

3. Results and Discussion

3.1. Physical Characterization

The crystal and phase information of synthetic materials were determined using X-ray diffraction (XRD) (Figure 1 and Figure S1). Broad peaks revealed the CuS XRD pattern. The typical diffraction peaks at 27.52° , 31.78° , and 53.04° were due to the crystal faces of (100), (103), and (108) interlayer reflections. MoS₂/Bi₂WO₆ diffraction peaks were found on the orthorhombic phase of Bi₂WO₆ (JCPDS No. 39-0256) and the hexagonal phase of MoS₂ (JCPDS No. 37-1492). However, typical CuS diffraction peaks did not appear in the

CuS/MoS₂/Bi₂WO₆ heterostructure. This may have been due to the low content of CuS in CuS/MoS₂/Bi₂WO₆.

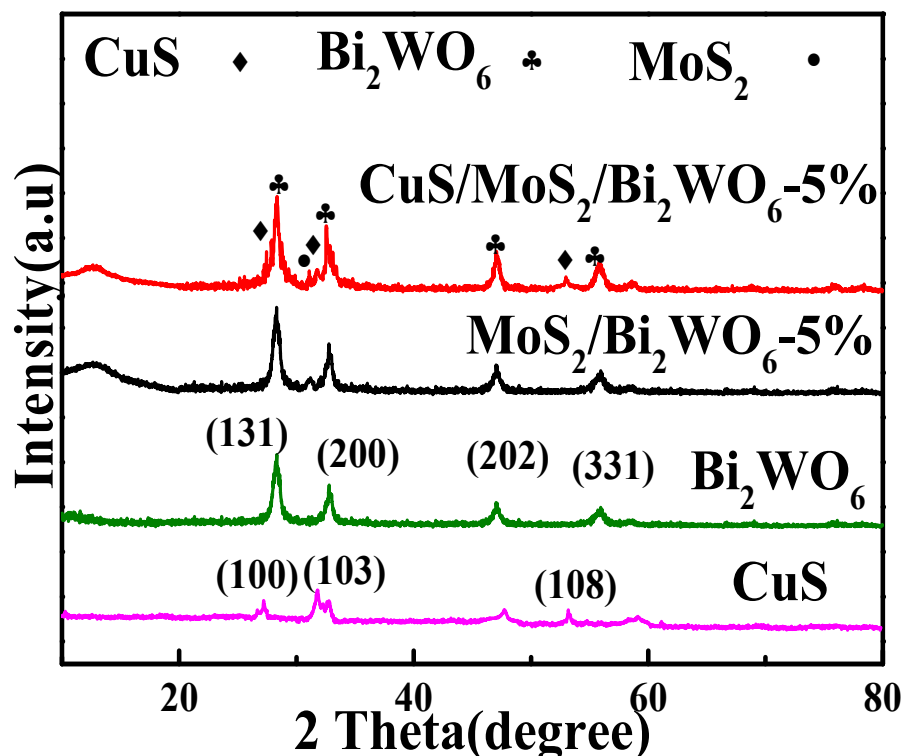


Figure 1. XRD patterns of CuS, Bi₂WO₆ and MoS₂/Bi₂WO₆-5%, CuS/MoS₂/Bi₂WO₆-5% nanocomposites.

XPS (Figure 2) confirmed the existence of Cu, S, O, Bi, W, and Mo in the chemical composition and valence band structure of CuS/MoS₂/Bi₂WO₆-5%. The high-resolution spectrum of Bi (Figure 2A) exhibited two distinct peaks for electrons in the Bi 4f orbitals at 158.8 and 164.2 eV under the distributions on Bi 4f_{7/2} and Bi 4f_{5/2} [31]. Figure 2B depicts the spectra for O 1s which is resolved into peak positions captured at 529.2 and 530.9 eV corresponding to the lattice oxygen in the microstructure and surface-adsorbed oxygen from the atmosphere, respectively [32]. The distinctive peaks at 34.9 eV and 36.9 eV for W 4f_{7/2} and W 4f_{5/2} (Figure 2C) were due to the presence of W atoms in the +6 oxidation state [33]. Figure 2D matches Mo 3d_{3/2} at 231.6 eV and Mo 3d_{5/2} at 228.4 eV with Mo⁴⁺ [34]. The XPS spectra of Cu 2p is shown in Figure 2E, with peaks centered at 932.4 eV (Cu 2p_{3/2}) and 952.4 eV (Cu 2p_{1/2}), indicating that Cu is present in the Cu²⁺ state [35,36]. According to Figure 2F, the doublet peak at 167.9 eV was a candidate for S 2p_{1/2}, while the peak at 162.5 eV was for S 2p_{3/2}, indicating the presence of metal sulfides [37,38]. These XPS data and Figures S3 and S4 were consistent with the composition CuS/MoS₂/Bi₂WO₆-5%.

Figure 3 represents the TEM images of their nanocomposite, and Figure 3A,B depict the recording of the Bi₂WO₆ and CuS/MoS₂/Bi₂WO₆-5% microstructure and high-resolution imaging. The picture demonstrates the microstructure's density, as indicated by the differential flakes protruding from the floral core structure. Additionally, to illuminate the growth planes in detail, high-resolution TEM (HR-TEM) in Figure 3D was used to calculate the interplanar spacing for 0.316 nm following the (131) plane of the Bi₂WO₆ structure, due to the lattice spacing of 0.328 and 0.158 for overgrown CuS and MoS₂, respectively, which arose from the (100) and (110) planes. Among Bi₂WO₆, CuS, and MoS₂, an explicit interface that benefited photocatalysis by forming a heterojunction enabled the efficient transfer of charge carriers.

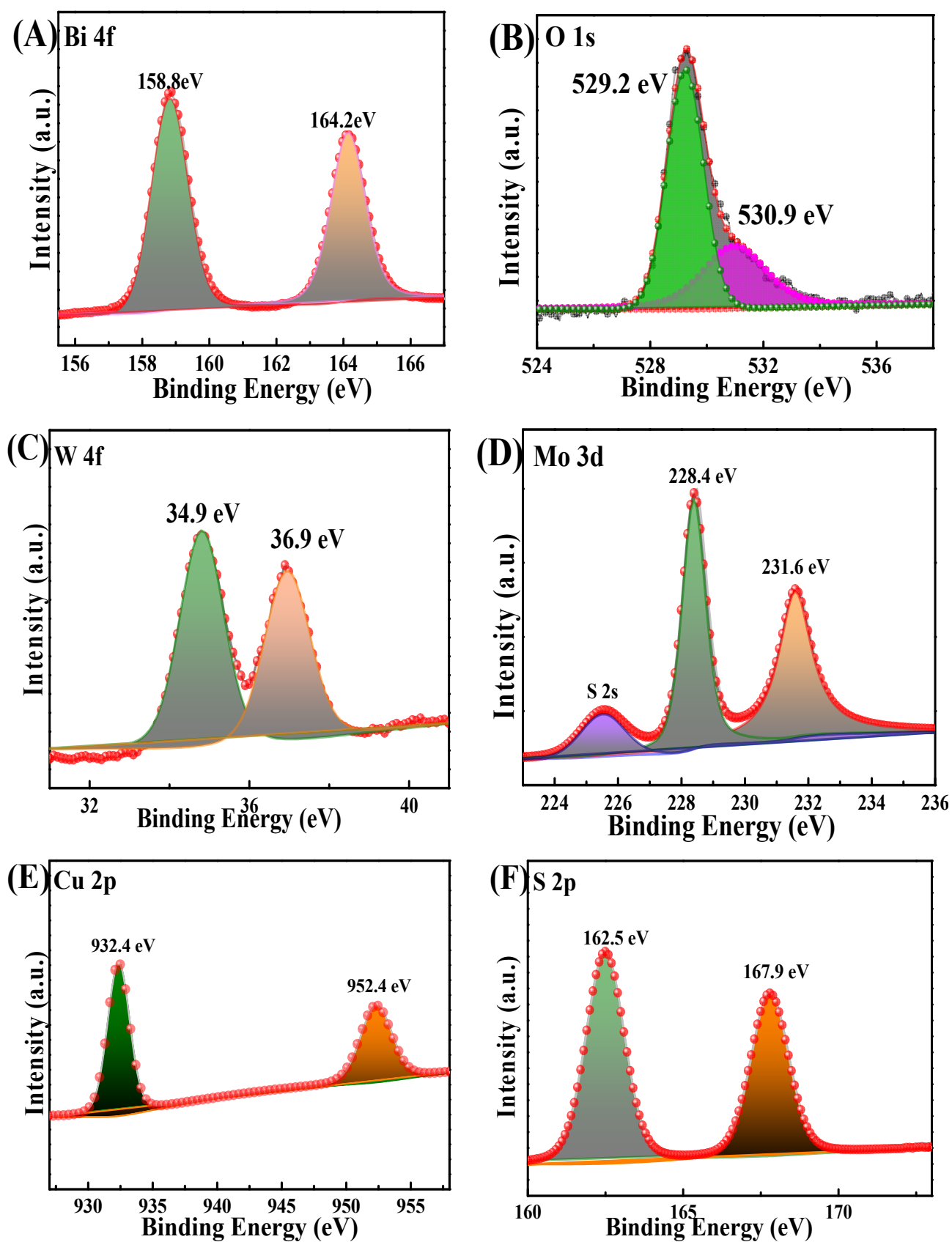


Figure 2. XPS spectra of Bi 4f (A), O 1s (B), W 4f (C), Mo 3d (D), Cu 2p (E), and S 2p (F) of CuS/MoS₂/Bi₂WO₆-5%.

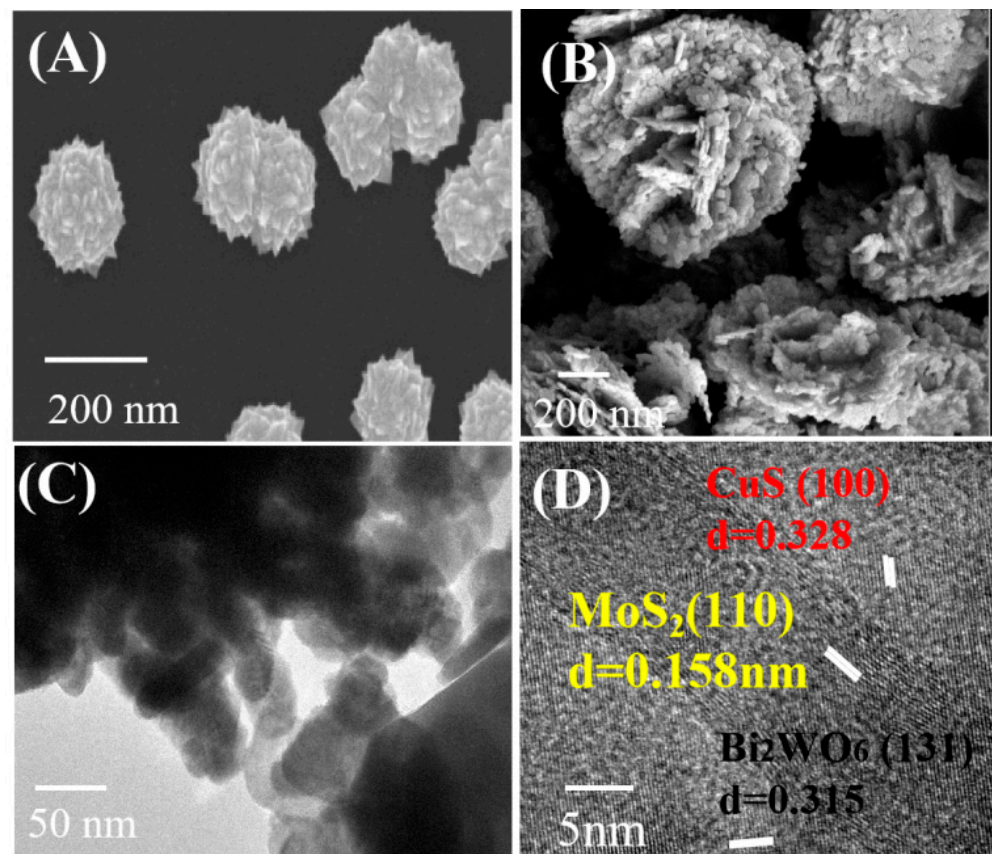


Figure 3. SEM images of Bi_2WO_6 (A) and SEM and TEM images $\text{CuS}/\text{MoS}_2/\text{Bi}_2\text{WO}_6$ -5% (B,C); HRTEM image of the $\text{CuS}/\text{MoS}_2/\text{Bi}_2\text{WO}_6$ -5% (D).

UV–visible diffuse reflectance spectroscopy was used to characterize the optical attributes of Bi_2WO_6 , $\text{MoS}_2/\text{Bi}_2\text{WO}_6$ -5%, and $\text{CuS}/\text{MoS}_2/\text{Bi}_2\text{WO}_6$ -5% (Figures 4 and S5). According to Figure 4A, after MoS_2 and CuS were included in the structure of Bi_2WO_6 , the visible light range offered a location for the broad absorption band. This might have been due to the enhanced visible-light absorptivity conferred by MoS_2 and CuS [39]. Accordingly, CuS - and MoS_2 -sensitized Bi_2WO_6 was designed to exhibit superior photocatalytic activity in the visible area due to heterojunction formation, sensitivity, and rapid charge transfer kinetics [40]. The room temperature photoluminescence emission spectra were measured in order to investigate the charge separation properties of Bi_2WO_6 , $\text{MoS}_2/\text{Bi}_2\text{WO}_6$ -5%, and $\text{CuS}/\text{MoS}_2/\text{Bi}_2\text{WO}_6$ -5%. Figure 4B depicts the photoluminescence emission spectrum at a 350 nm excitation wavelength. Bi_2WO_6 was seen to have a higher characteristic spectrum between the wavelengths of 500 and 680 nm, which was caused by charge carrier recombination, the emission peak position in the range of 550–600 nm shift to the right when adding CuS to the composite $\text{MoS}_2/\text{Bi}_2\text{WO}_6$, which is due to the smaller energy band of the composite material, and the red shift of the emission peak occurred [41]. Obviously, the peak intensity of $\text{MoS}_2/\text{Bi}_2\text{WO}_6$ -5%, and $\text{CuS}/\text{MoS}_2/\text{Bi}_2\text{WO}_6$ -5% was significantly lower than that of Bi_2WO_6 , suggesting that the integration of CuS and MoS_2 could reduce photo-generated charge carrier recombination. In general, reduced intensity indicates improved electron–hole separation efficiency due to the carriers’ greater lifespan and higher PEC.

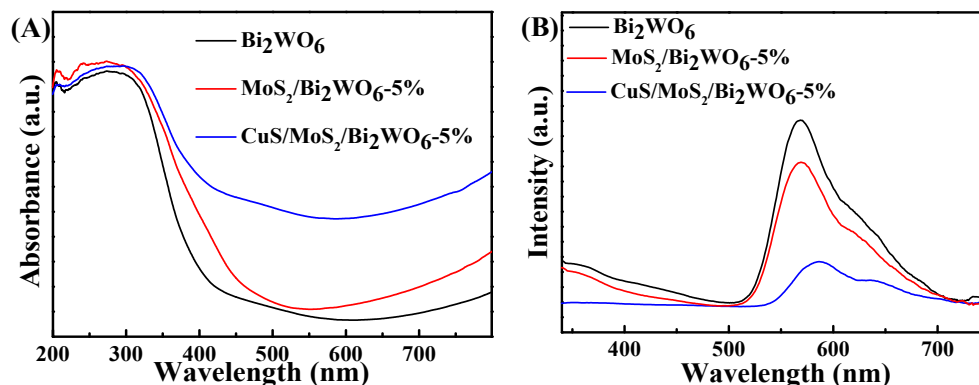


Figure 4. (A) UV-Vis absorbance spectra and (B) photoluminescence spectra of Bi₂WO₆, MoS₂/Bi₂WO₆-5%, and CuS/MoS₂/Bi₂WO₆-5%.

3.2. Theoretical Calculations

DFT determined the density of states (DOS) and energy band structures for Bi₂WO₆ and CuS/MoS₂/Bi₂WO₆-5% (Figure 5). Clearly, Bi₂WO₆ serves as the photocatalytic material of an indirect band-gap semiconductor since the valence band maximum (VBM) and conduction band minimum (CBM) are located at diverse high symmetry points, as seen between CBM at Γ -point and VBM at X-point. Calculations yielded a Bi₂WO₆ band gap of 1.86 eV. Notably, the band gaps were significantly lower compared with the literature (2.56 eV for Bi₂WO₆) [35], which was likely due to the defected GGA function (Figure 5A,B). In the photocatalyst, photogenerated h⁺ and e⁻ were efficiently isolated and quickly transported onto surfaces. Figure 5B,D shows the DOS with CuS/MoS₂/Bi₂WO₆-5%, which indicated that CuS and MoS₂ gain charges as electron trapping and shuttling sites, suppress the recombination of electrons/holes, and promote electron separation and transfer [36].

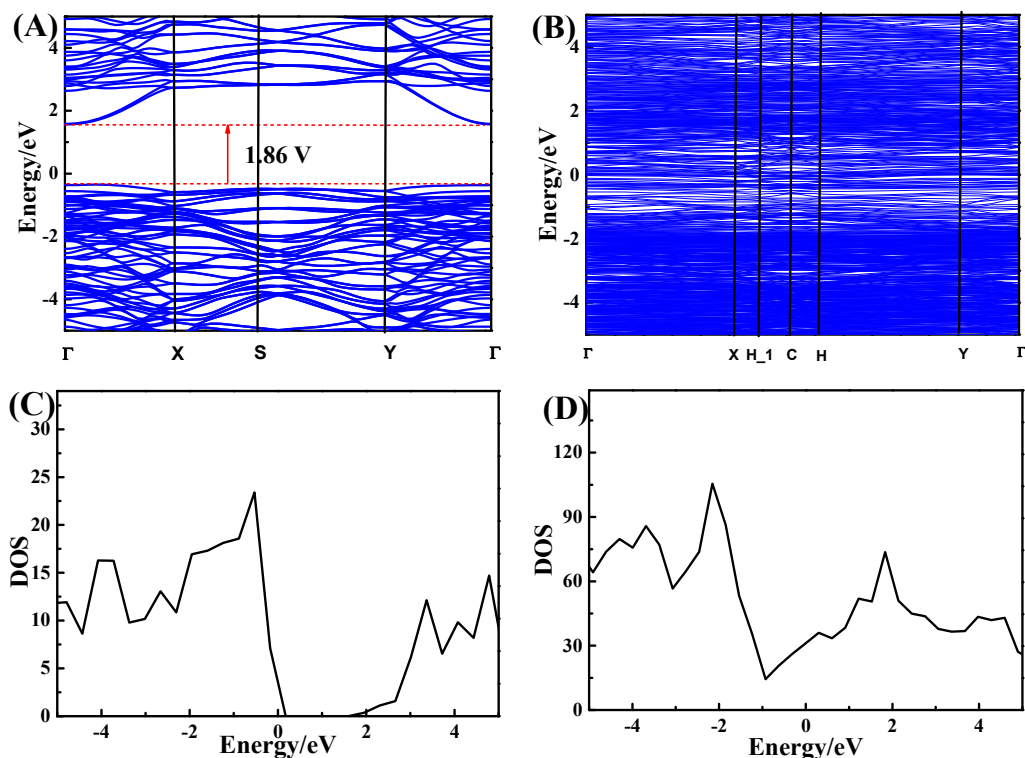


Figure 5. Band structures for (A) Bi₂WO₆ and (B) CuS/MoS₂/Bi₂WO₆ and DOS for (C) Bi₂WO₆ and (D) CuS/MoS₂/Bi₂WO₆-5%.

3.3. Photoelectrochemical Sensor

Electrochemical impedance spectroscopy (EIS) was used to analyze the electrode contact properties. The impedance spectra following the various biosensor fabrication procedures are shown in Figure 6A. Every impedance spectrum contained a high-frequency semicircle and a low-frequency linear part. The semicircle represented a finite electron transfer mechanism, whereas the linear section represented a finite diffusion process. The semicircle's diameter illustrated the restricted diffusion of the redox probe into the electrode interface, with the exact quantities as the electron transfer resistance (R_{et}). The impedance spectra of the $\text{MoS}_2/\text{Bi}_2\text{WO}_6$ electrode represented a tiny semicircle (Figure S2), which corresponded to a modest R_{et} value. Because of the poor conductivity of this semiconductor, the R_{et} (curve I) for $\text{CuS}/\text{MoS}_2/\text{Bi}_2\text{WO}_6$ -5% increased. As a result of the decreased electron transport efficiency, the R_{et} saw extensive growth when CS was added (curve II). During the aptamer fixing, the R_{et} increased further (curves III), owing to the poor conductivity of these organic molecules and resistance from the negatively charged layer of phosphate groups. Then, after incubating the electrode with DCF, the R_{et} increased dramatically (curve IV), indicating DCF contact with the electrode surface. The biosensor was successfully created due to the potential shift in R_{et} .

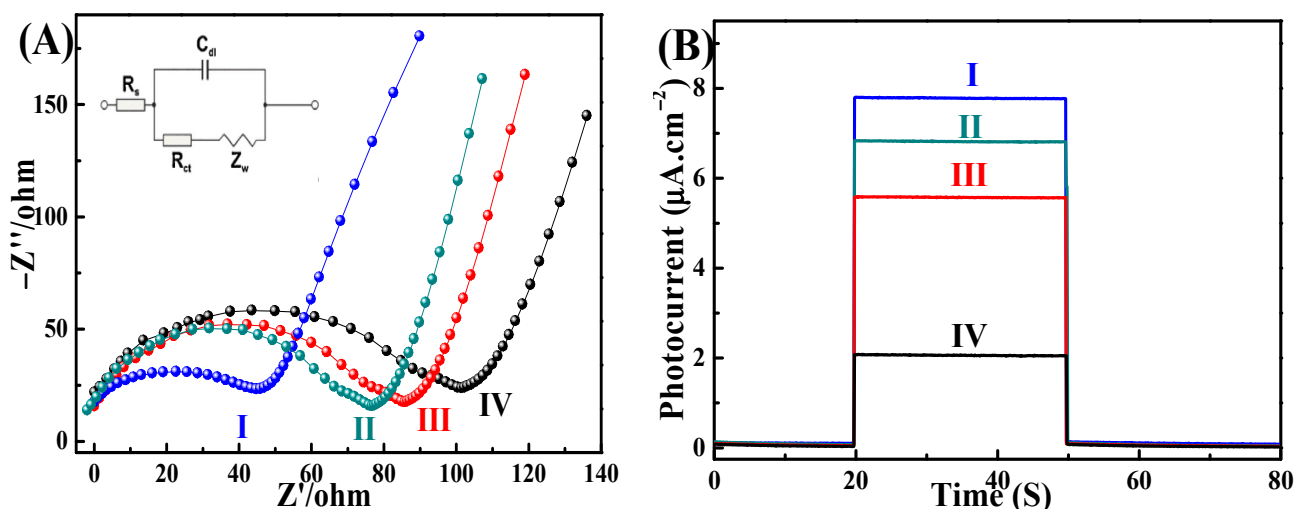
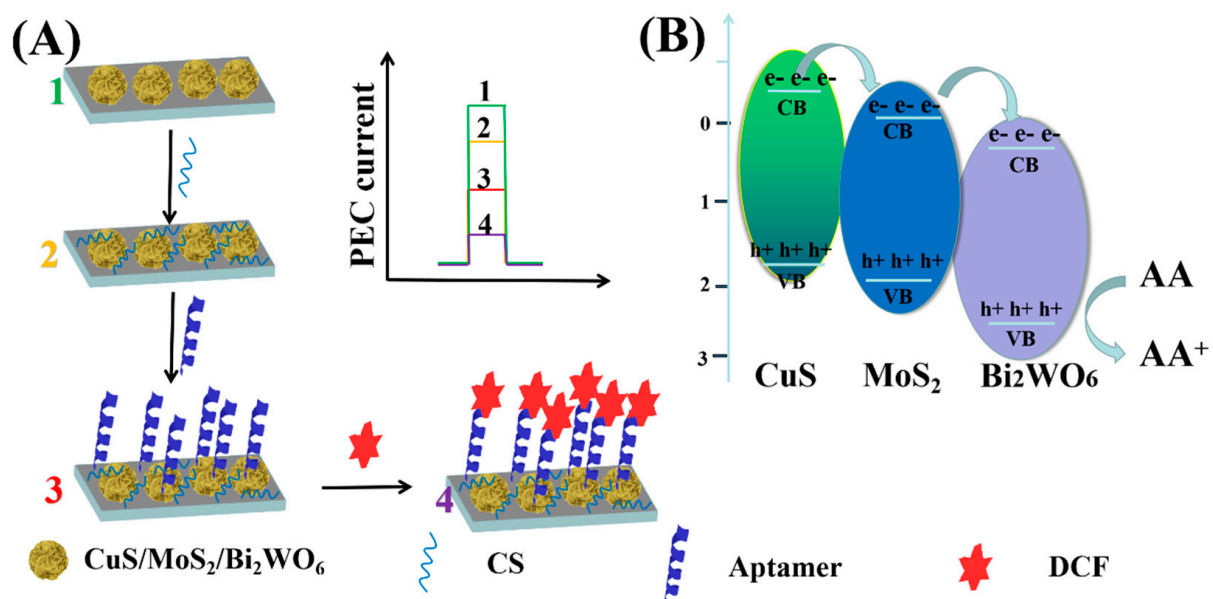


Figure 6. Nyquist plots (A) and PEC responses (B) of different electrodes: (I) $\text{CuS}/\text{MoS}_2/\text{Bi}_2\text{WO}_6$ -5%, (II) $\text{CS}/\text{CuS}/\text{MoS}_2/\text{Bi}_2\text{WO}_6$ -5%, (III) aptamer/ $\text{CS}/\text{CuS}/\text{MoS}_2/\text{Bi}_2\text{WO}_6$ -5%, and (IV) DCF/aptamer/ $\text{CuS}/\text{MoS}_2/\text{Bi}_2\text{WO}_6$ -5%. The EIS spectra were achieved in 0.1 M KCl containing 5 mM $\text{Fe}(\text{CN})_6^{3-/4-}$.

The low photocurrent intensity shown by the $\text{CuS}/\text{MoS}_2/\text{Bi}_2\text{WO}_6$ -5% electrode resulted from a high electron–hole pair recombination rate (Figure 6B). Because of the expected acceleration of electron transport, the photocurrent intensity increased significantly after adding CuS nanoparticles (curve II). When the electron donor solution of ascorbic acid (AA) and the electrode surface of $\text{CuS}/\text{MoS}_2/\text{Bi}_2\text{WO}_6$ -5% met with the impeded electron exchange, the photocurrent density gradually decreased when CS and aptamer (curves III and IV) were added. The aptamer sensor was found to be successfully constructed. The binding of DCF resulted in increased photocurrent (curve IV), which most likely resulted in DCF oxidation and electron transport to the counter electrode.

When the aptamer recognizes the detection target, the magnitude of change in the photocurrent plays a critical role in the sensitivity of the photoelectrochemical aptamer analysis. This study shows the aptamer analysis method's design. The photocurrent response characterization experiments described above specialized in ultra-high sensitivity, which stems from the two elements listed below. The schematic diagram could be used to represent the preparation process of the intended aptamer sensor in order to obtain an

explicit interpretation (Scheme 2) [42–44]. In the absence of DCF, the electron transfer rate may have been considerably enhanced because the CuS/MoS₂/Bi₂WO₆-5% composite could absorb the energy of the UV and light source. As an electron donor, ascorbic acid could consume holes in the semiconductor material, reduce the electron–hole recombination rate of the material, and could amplify the photocurrent signal, thereby reducing the error caused by the small change in the current data after adding DCF. Furthermore, the sensing electrode altered the recombination of electron–hole pairs and showed a noticeable photocurrent response. Further oxidation was carried out under the photogenerated holes when the aptamer connected with the target DCF. As a result, the sensing electrode's current was accelerated, resulting in a significant increase in photocurrent intensity.



Scheme 2. (A) Fabrication process of PEC sensor for DCF detection under light irradiation and (B) the electron-transfer process of CuS/MoS₂/Bi₂WO₆-5% nanocomposites.

3.4. The Influence of Effective Parameters on the Detection of DCF

Figure 7A depicted the examination of the applied potential selection. Due to the difference in potential between -0.2 V and 0.3 V, the aptamer/CS/CuS/MoS₂/Bi₂WO₆-5% and DCF/aptamer/CS/CuS/MoS₂/Bi₂WO₆-5% were tested in the dark or in the presence of light. When comparing photocurrent to dark in different currents, the photocurrent decreased dramatically when the potential changed from -0.2 V to 0.1 V. However, it was shown to exhibit a modest drop when the potential difference was between 0.1 V and 0.3 V. As a result, 0.1 V may be used as the PEC matching voltage.

During the detection process, the pH of the electrolyte, a critical component of the PEC performance, must be optimized (Figure 7B). The photocurrent increased as the pH value of the electrolyte was increased from 5 to 7. As the pH value decreased from 7 to 9, the photocurrent decreased. Because the neutral environment presumably benefits the aptamer activity, it could achieve its maximum value at pH = 7.

According to Figure 7C, to conduct in-depth research on the long-term stability of DCF detection based on the aptamer/CS/CuS/MoS₂/Bi₂WO₆-5% sensor in the absence and presence of DCF, in the same solution, a sensor coated with aptamer/CS/CuS/MoS₂/Bi₂WO₆-5% was used to measure DFC every 5 days. After 20 days, there was no substantial change in the aptamer/CS/CuS/MoS₂/Bi₂WO₆-5% sensor's photocurrent response to DCF. As a result, it was demonstrated that the composite sensor was designed to emphasize improved stability. To achieve optimal sensitivity, the aptamer concentration (0.1 – 2 $\mu\text{mol/L}$) is optimized in Figure 7D, which demonstrates the electrode's greatest photocurrent at a concentration of 1.0 $\mu\text{mol/L}$. As a result, this study approved a 1.0 $\mu\text{mol/L}$ aptamer concentration.

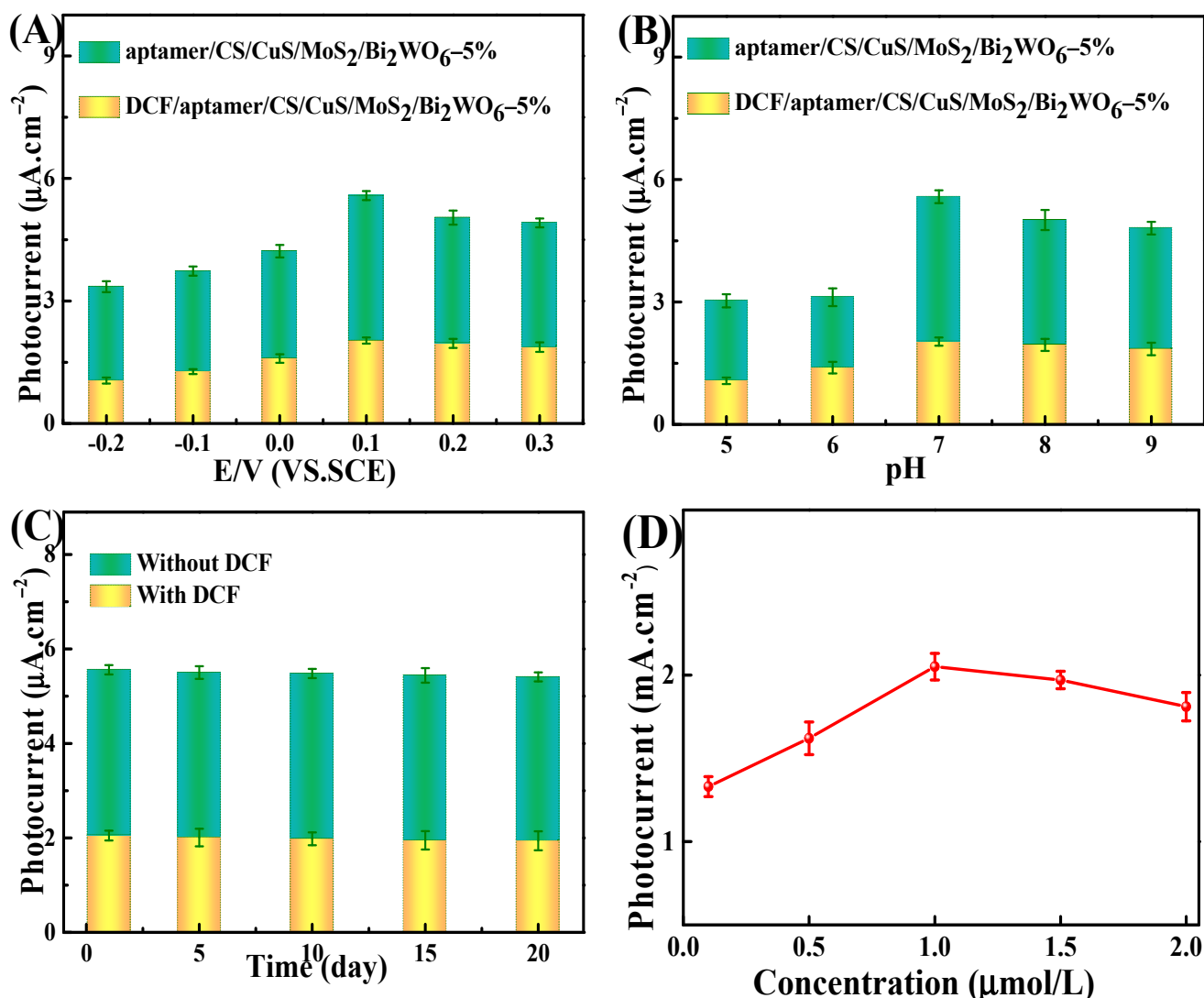


Figure 7. (A) the applied potential selection, (B) the electrolyte of pH selection, (C) stability test of PEC aptasensor, and (D) impacts of aptamer concentration on the photocurrent response of the aptasensor based on aptamer/CS/CuS/MoS₂/Bi₂WO₆-5%.

Aptamer/CS/CuS/MoS₂/Bi₂WO₆-5% was used to analyze DCF concentrations under optimized circumstances. According to Figure 8A, the photocurrent increased in proportion to the DCF concentration due to the aptamer's specific binding to DCF. The generated DCF–aptamer complexes on the sensor interface reduced the steric barrier for electron-donor diffusion, resulting in a drop in photocurrent. Within the concentration range of 0.1 to 500 nM (Figure 8B), the photocurrent change followed a linear relationship with the DCF concentration, resulting in a detection limit of 0.03 nM (S/N = 3). $PI = 1.278 + 1.316\log C$ was used as the calibration regression equation (nM). A correlation coefficient (R^2) of 0.9965 was obtained. The suggested sensor's performance, which included additional previously reported characteristics, demonstrated a substantially lower detection limit within a comparable linear range (Table S1).

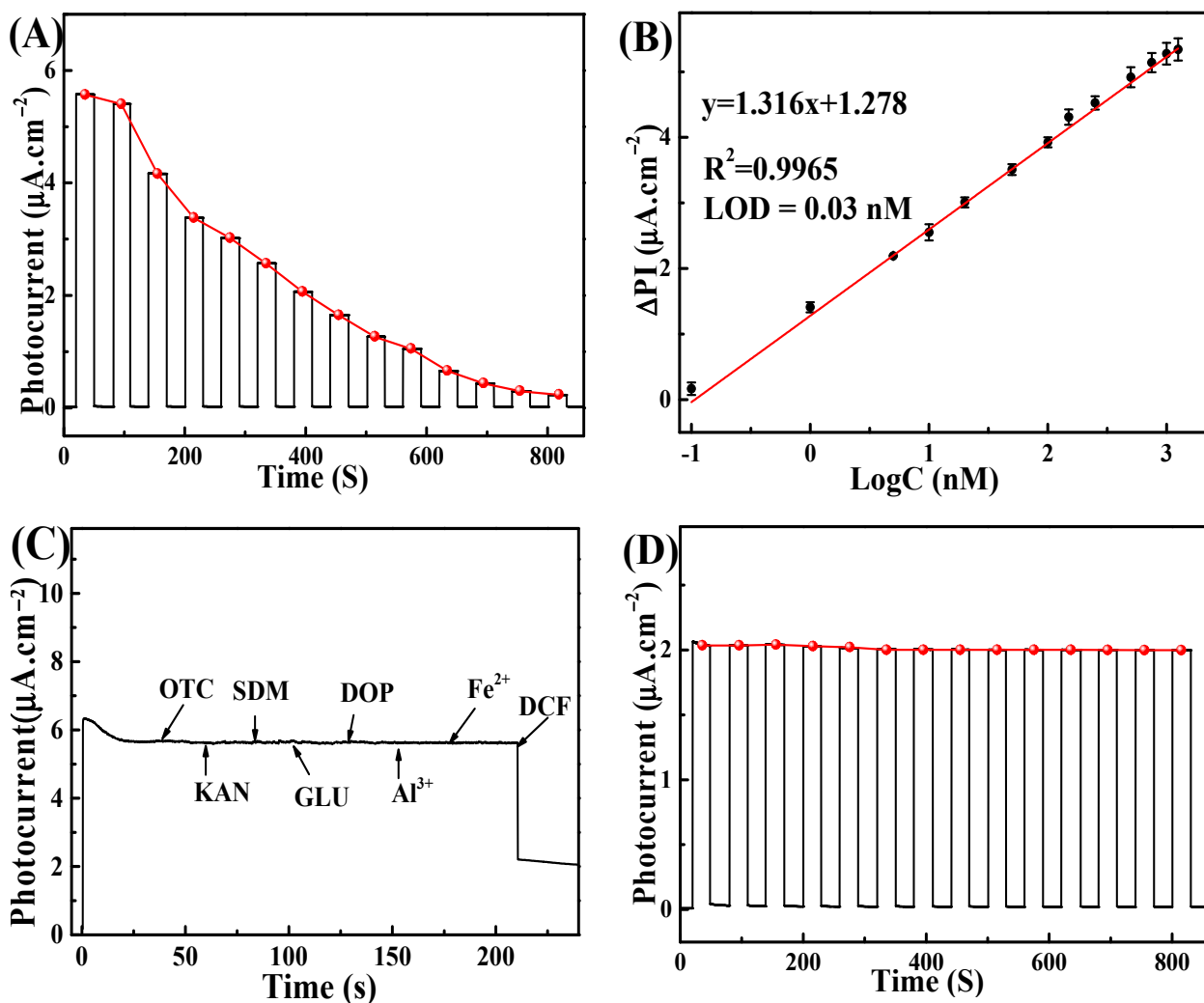


Figure 8. (A) Photocurrent responses of the aptamer/CS/CuS/MoS₂/Bi₂WO₆-5% at various DCF levels in PBS (0.1 M, pH 7.0) at a bias potential of 0.1 V: (0.1–500 nM). (B) The linear calibration curve for STR determination. (C) Selectivity and (D) stability of the PEC sensor based on aptamer/CS/CuS/MoS₂/Bi₂WO₆-5% for DCF detection.

According to Figure 8C, after waiting for the photocurrent of aptamer/CS/CuS/MoS₂/Bi₂WO₆-5% to stabilize, additional interfering agents, including kanamycin (KAN), sulfadimethoxine (SDM), ochratoxin A (OTA), dopamine (DOP), glucose (GLU), Al³⁺, and Fe²⁺, were added, and the change in the photocurrent after stabilization was investigated. The photocurrent showed no discernible change in the coexisting ion supplement. Additionally, it demonstrated high selectivity for DCF detection using aptamer/CS/CuS/MoS₂/Bi₂WO₆-5%. Figure 8D demonstrates the stability of the aptamer/CS/CuS/MoS₂/Bi₂WO₆-5%-based PEC sensor for DCF detection. The repeated photoexcitation procedure monitored the PEC sensor every 800 seconds. The observation demonstrated that the photocurrent and dark current remained stable throughout the time, indicating the reliability of the PEC sensor during the detection of DCF. As discussed before, the aptamer/CS/CuS/MoS₂/Bi₂WO₆-5%-based sensor has exceptional stability, repeatability, and DCF stability.

3.5. Real Sample Analysis

By using a standard addition technique and comparing it to HPLC readings, DCF in tap water was analyzed to determine the practical applicability of the created biosensor. To begin, DCF capsules were pulverized to a powder in an agate mortar. Following that,

different volumes of powder were dissolved in tap water to create solutions with varying concentrations. Then, on a quantitative basis, the resulting solutions were analyzed, as shown in Table 1. Consistent with the HPLC recovery (95.00–101.82%), the aptasensor recovery was between 97.00 and 102.33%, demonstrating that the PEC aptasensor can be utilized to detect DCF in realistic samples.

Table 1. Determination of DCF in river water samples based on the constructed PEC sensing platform.

Sample	PEC Aptasensor				ICP-MS		
	Applied (nM)	Found (nM)	Recovery (%)	RSD (%)	Found (nM)	Recovery (%)	RSD (%)
1	1.00	0.97	97.00	2.39	0.95	95.00	3.14
2	10.00	10.07	100.70	2.71	10.02	100.20	2.55
3	50.00	49.88	99.76	3.21	49.85	99.70	2.01
4	100.00	102.33	102.33	2.92	101.82	101.82	3.11
5	200.00	203.52	101.76	3.47	202.89	101.44	3.52

4. Conclusions

To summarize, our study developed a new visible-light PEC aptamer sensor based on CuS/MoS₂/Bi₂WO₆ nanocomposites for DCF detection. DCF is clinically used for osteoarthritis and non-articular rheumatism, in which the PEC aptamer sensor will have great application prospects. The CS/CuS/MoS₂/Bi₂WO₆ heterostructure plays a critical role in the photocurrent response of the PEC sensor, which operated across a broad linear range of 0.1–500 nM with a detection limit of 0.03 nM, exceeding the detection limit and linearity of typically modified electrodes. This novel PEC sensing strategy provided an ultra-sensitive sensor with high selectivity and stability for DCF detection. At the moment, our focus is on miniaturizing this technology to be used in more areas.

Supplementary Materials: The following supporting information can be downloaded at: <https://www.mdpi.com/article/10.3390/nano12162834/s1>, Figure S1: XRD patterns of MoS₂, MoS₂/Bi₂WO₆-2% and MoS₂/Bi₂WO₆-5%, MoS₂/Bi₂WO₆-7% nanocomposites; Figure S2: Nyquist plots (A) and PEC responses (B) of different electrodes: (I) Bi₂WO₆, (II) MoS₂/Bi₂WO₆-2%, (III) MoS₂/Bi₂WO₆-5% and (IV) MoS₂/Bi₂WO₆-7%; Figure S3: EDS spectrum of CuS/MoS₂/Bi₂WO₆-5% microstructures; Figure S4: FT-IR spectra of the CuS/MoS₂/Bi₂WO₆-5% composites; Figure S5: Plots of $(\alpha h\nu)^{1/2}$ vs. photon energy (hν) for Bi₂WO₆; Table S1: Comparison of analytical performances of the CuS/MoS₂/Bi₂WO₆ electrodes with the typical reported methods. References [11,45–49] are cited in the Supplementary Materials.

Author Contributions: Investigation, H.G.; Methodology, H.G.; Project administration, Y.H.; Supervision, J.L.; Writing—original draft, Y.H.; Writing—review & editing, J.L. All authors have read and agreed to the published version of the manuscript.

Funding: This work was supported by the 2019 National Natural Science Foundation of China General Project (31770917).

Institutional Review Board Statement: Not applicable.

Informed Consent Statement: Not applicable.

Data Availability Statement: The data presented in this study are available on request from the corresponding author.

Conflicts of Interest: The authors declare no conflict of interest.

References

- Cheng, C.; Bai, X.X.; Zhang, J.; He, Q. Intensified interactions of triclosan and diclofenac mitigation and nitrogen removal in manganese oxide constructed wetlands. *Chem. Eng. J.* **2022**, *433*, 134493. [CrossRef]
- Elbalkiny, H.T.; Yehia, A.M.; Riad, S.M.; Elsharty, Y.S. Potentiometric diclofenac detection in wastewater using functionalized nanoparticles. *Microchem. J.* **2019**, *145*, 90–95. [CrossRef]

3. Nguyen, T.T.K.; Vu, T.T.; Anquetin, G.; Tran, H.V.; Reisberg, S.; Mattana, V.N.G.; Nguyen, Q.V.; Lam, T.D.; Pham, M.C.; Piro, B. Enzyme-less electrochemical displacement heterogeneous immunosensor for diclofenac detection. *Biosens. Bioelectron.* **2017**, *97*, 246–252. [[CrossRef](#)] [[PubMed](#)]
4. Steinke, N.; Rio, M.; Wuchrer, R.; Schuster, C.; Ljasenko, E.; Knopp, D.; Gerlach, G.; Härtling, T. Detection of diclofenac molecules by planar and nanostructured plasmonic sensor substrates. *Sens. Actuators B Chem.* **2018**, *254*, 749–754. [[CrossRef](#)]
5. Seguro, I.; Pacheco, J.G.; Matos, C.D. Low Cost, Easy to Prepare and Disposable Electrochemical Molecularly Imprinted Sensor for Diclofenac Detection. *Sensors* **2021**, *21*, 1975. [[CrossRef](#)] [[PubMed](#)]
6. Ecke, A.; Westphalen, T.; Hornung, J. A rapid magnetic bead-based immunoassay for sensitive determination of diclofenac. *Anal Bioanal. Chem.* **2022**, *414*, 1563–1573. [[CrossRef](#)]
7. Shishov, A.; Nechaeva, D.; Bulatov, A. HPLC-MS/MS determination of non-steroidal anti-inflammatory drugs in bovine milk based on simultaneous deep eutectic solvents formation and its solidification. *Microchem. J.* **2019**, *150*, 104080. [[CrossRef](#)]
8. Killedar, L.; Ilager, D.; Shetti, N.P.; Aminabhavi, T.M.; Reddy, K.R. Synthesis of ruthenium doped titanium dioxide nanoparticles for the electrochemical detection of diclofenac sodium. *J. Mol. Liq.* **2021**, *340*, 116891. [[CrossRef](#)]
9. Beilinson, R.M.; Yavisheva, A.A.; Medyantseva, E.P. Amperometric Tyrosinase Biosensors Modified by Nanomaterials of Different Nature for Determining Diclofenac. *J. Anal. Chem.* **2021**, *76*, 653–659. [[CrossRef](#)]
10. Shanbhag, M.M.; Ilager, D.; Mahapatra, S.; Shetti, N.P.; Chandra, P. Amberlite XAD-4 based electrochemical sensor for diclofenac detection in urine and commercial tablets. *Mater. Chem. Phys.* **2021**, *273*, 125044. [[CrossRef](#)]
11. Okoth, O.K.; Yan, K.; Feng, J.; Zhang, J.D. Label-free photoelectrochemical aptasensing of diclofenac based on gold nanoparticles and graphene-doped CdS. *Sens. Actuators B Chem.* **2018**, *256*, 334–341. [[CrossRef](#)]
12. Wang, Q.; Jiang, M.; Zhang, L. Label-free and visible-light driven photoelectrochemical sensor with CuCo₂O₄@CoO Core-shell hybrid rod as photoanode for selective sensing diclofenac. *Electrochim. Acta* **2021**, *397*, 139239. [[CrossRef](#)]
13. Liao, X.L.; Li, T.T.; Ren, H.T.; Mao, Z.Y.; Zhang, X.F.; Lin, J.H.; Lou, C.W. Photoelectrochemical aptasensor driven by visible-light based on BiFeO₃@TiO₂ heterostructure for microcystin-LR detection. *Microchem. J.* **2022**, *176*, 107201. [[CrossRef](#)]
14. Niu, X.K.; Lu, C.T.; Su, D.; Wang, F.; Tan, W.H.; Qu, F.L. Construction of a Polarity-Switchable Photoelectrochemical Biosensor for Ultrasensitive Detection of miRNA-141. *Anal. Chem.* **2021**, *93*, 13727–13733. [[CrossRef](#)] [[PubMed](#)]
15. Mao, X.Y.; Zhang, C.S. A microfluidic cloth-based photoelectrochemical analytical device for the detection of glucose in saliva. *Talanta* **2022**, *238*, 123052. [[CrossRef](#)]
16. Yan, P.C.; Xu, L.; Cheng, X.M.; Qian, J.C.; Li, H.N.; Xia, J.X.; Zhang, Q.; Hua, M.Q.; Li, H.M. Photoelectrochemical monitoring of phenol by metallic Bi self-doping BiOI composites with enhanced photoelectrochemical performance. *J. Electroanal. Chem.* **2017**, *804*, 64–71. [[CrossRef](#)]
17. Yan, P.C.; Xu, L.; Jiang, D.S.; Li, H.N.; Xia, J.X.; Zhang, Q.; Hua, M.Q.; Li, H.M. Photoelectrochemical monitoring of ciprofloxacin based on metallic Bi self-doping BiOBr nanocomposites. *Electrochim. Acta* **2018**, *259*, 873–881. [[CrossRef](#)]
18. Zheng, X.; Zhang, X.D.; Cai, Y.P.; Zhao, S.; Wang, S.G. Efficient degradation of bisphenol A with MoS₂/BiVO₄ hetero-nanoflower as a heterogenous peroxymonosulfate activator under visible-light irradiation. *Chemosphere* **2022**, *289*, 133158. [[CrossRef](#)]
19. Alfaihi, B.Y.; Tahir, A.A.; Wijayantha, K.G.U. Fabrication of Bi₂WO₆ photoelectrodes with enhanced photoelectrochemical and photocatalytic performance. *Sol. Energ. Mat. Sol. C.* **2019**, *195*, 134–141. [[CrossRef](#)]
20. Dong, G.J.; Zhang, Y.J.; Bi, Y.P. The synergistic effect of Bi₂WO₆ nanoplates and Co₃O₄ cocatalysts for enhanced photoelectrochemical properties. *J. Mater. Chem. A* **2017**, *5*, 20594–20597. [[CrossRef](#)]
21. Tatá, L.M.J.; Carvajal, D.; Núñez, O.; Scharifker, B.R.; Mostany, J.; Borrás, C.; Cabrerizo, F.M.; Vargas, R. Photocatalysis and photoelectrochemical glucose oxidation on Bi₂WO₆: Conditions for the concomitant H₂ production. *Renew. Energ.* **2020**, *152*, 974–983.
22. Tang, X.; Guo, X.L.; Chen, Z.T.; Liu, Y.Y.; Zhang, W.J.; Wang, Y.X.; Zheng, Y.M.; Zhang, M.; Peng, Z.B.; Li, R.; et al. Facile preparation of Cu₂O nanoparticles/Bi₂WO₆/rGO hybrid with enhanced photoelectrochemical performance. *Appl. Surf. Sci.* **2020**, *510*, 145447. [[CrossRef](#)]
23. Huang, W.; Cheng, Y.; Fei, X. Designing of CuS growing on Bi₂WO₆ nanosheet heterostructures based on a photoelectrochemical aptasensor for detecting ofloxacin. *Microchim. Acta* **2020**, *187*, 583. [[CrossRef](#)] [[PubMed](#)]
24. Li, Y.J.; Yu, X.G.; Li, R.Q.; Zhao, F.; Liu, G.B.; Wang, X. Selective and sensitive visible-light-prompt photoelectrochemical sensor of paracetamol based on Bi₂WO₆ modified with Bi and copper sulfide. *RSC Adv.* **2021**, *11*, 2884–2891. [[CrossRef](#)] [[PubMed](#)]
25. Varunkumar, K.; Sellappan, R. Photoelectrochemical behaviour of CuBi₂O₄@MoS₂ photocathode for solar water splitting. *Mater. Chem. Phys.* **2021**, *261*, 124245. [[CrossRef](#)]
26. PesciOrcid, F.M.; Sokolikova, M.S.; Grotta, C.; Sherrell, P.C.; Reale, F.; Sharda, K.; Ni, N.; Palczynski, P.; Mattevi, C. MoS₂/WS₂ Heterojunction for Photoelectrochemical Water Oxidation. *ACS Catal.* **2017**, *7*, 4990–4998.
27. Liu, X.Q.; Huo, X.H.; Liu, P.P.; Tang, Y.F.; Xu, J.; Liu, X.H.; Zhou, Y.M. Assembly of MoS₂ nanosheet-TiO₂ nanorod heterostructure as sensor scaffold for photoelectrochemical biosensing. *Electrochim. Acta* **2017**, *242*, 327–336. [[CrossRef](#)]
28. Du, J.M.; Yang, M.K.; Zhang, F.F.; Cheng, X.C.; Wu, H.R.; Qin, H.C.; Jian, Q.S.; Lin, X.L.; Li, K.D.; Kang, D.J. Enhanced charge separation of CuS and CdS quantum-dot-cosensitized porous TiO₂-based photoanodes for photoelectrochemical water splitting. *Ceram. Int.* **2018**, *44*, 3099–3106. [[CrossRef](#)]
29. Zhang, X.Y.; Li, M.Y.; He, L.M.; Tian, D.D.; Zhang, L.J.; Zhang, J.H.; Liu, M. Highly sensitive and selective photoelectrochemical sensor for mercury(II) detection based on efficient Bi₂MoO₆ photoanode decorated with CuS. *J. Alloy. Compd.* **2021**, *864*, 157905. [[CrossRef](#)]

30. Wang, Y.F.; Bai, L.; Wang, Y.L.; Qin, D.D.; Shan, D.L.; Lu, X.Q. Ternary nanocomposites of Au/CuS/TiO₂ for an ultrasensitive photoelectrochemical non-enzymatic glucose sensor. *Analyst* **2018**, *143*, 1699–1704. [[CrossRef](#)]
31. Hu, W.; Wu, F.; Liu, W. Construction of S-scheme heterojunction by doping Bi₂WO₆ into Bi₂O₃ for efficiently enhanced visible-light photocatalytic performance. *J Mater Sci.* **2022**, *57*, 4265–4282. [[CrossRef](#)]
32. Yang, M.Y.; Xu, T.T.; Jin, X.Q.; Shen, Q.; Sun, C.Y. Oxygen vacancies enriched Bi₂WO₆ for enhanced decabromodiphenyl ether photodegradation via C-Br bond activation. *Appl. Surf. Sci.* **2022**, *581*, 152439. [[CrossRef](#)]
33. Mirhosseini, H.; Mostafavi, A.; Shamspur, T.; Sargazi, G. Fabrication of an efficient ternary TiO₂/Bi₂WO₆ nanocomposite supported on g-C₃N₄ with enhanced visible-light- photocatalytic activity: Modeling and systematic optimization procedure. *Arab. J. Chem.* **2022**, *15*, 103729. [[CrossRef](#)]
34. Roy, K.; Maitra, S.; Ghosh, D.; Kumar, P.; Devi, P. 2D-Heterostructure assisted activation of MoS₂ basal plane for enhanced photoelectrochemical hydrogen evolution reaction. *Chem. Eng. J.* **2022**, *435*, 134963. [[CrossRef](#)]
35. Wen, Y.X.; Sheng, M.Q.; Hong, L.C.; Nian, Q.L.; Li, B. Y-type DNA structure stabilized p-type CuS quantum dots to quench photocurrent of ternary heterostructure for sensitive photoelectrochemical detection of miRNA. *Sens. Actuators B Chem.* **2021**, *329*, 129257. [[CrossRef](#)]
36. Zou, L.; Yang, L.; Zhan, Y. Photoelectrochemical aptasensor for thrombin based on Au-rGO-CuS as signal amplification elements. *Microchim. Acta* **2020**, *187*, 433. [[CrossRef](#)] [[PubMed](#)]
37. Tang, Y.F.; Chai, Y.; Liu, X.Q.; Li, L.L.; Yang, L.W.; Liu, P.P.; Zhou, Y.M.; Ju, H.X.; Cheng, Y.Z. A photoelectrochemical aptasensor constructed with core-shell CuS-TiO₂ heterostructure for detection of microcystin-LR. *Biosens. Bioelectron.* **2018**, *117*, 224–231. [[CrossRef](#)] [[PubMed](#)]
38. Yang, H.M.; Wang, J.J.; Yu, H.H.; Li, X.; Li, Z.L.; Cui, K.; Zhang, L.; Ge, S.G.; Yu, J.H. FeOOH/Cu₂O/CuS photocathode-enabled simultaneous promotion on charge carrier separation and electron acceptor reduction for lab-on-paper homogeneous cathodic photoelectrochemical bioassay. *Chem. Eng. J.* **2022**, *430*, 132846. [[CrossRef](#)]
39. Dagar, P.; Kumar, S.; Ganguli, A.K. Effect of Mn²⁺ incorporation on the photoelectrochemical properties of BiVO₄. *New J. Chem.* **2022**, *46*, 2875–2886. [[CrossRef](#)]
40. Peerakiatkhajohn, P.; Yun, J.H.; Butburee, T.; Nisspad, W.; Thaweesak, S. Surface plasmon-driven photoelectrochemical water splitting of a Ag/TiO₂ nanoplate photoanode. *RSC Adv.* **2022**, *12*, 2652–2661. [[CrossRef](#)] [[PubMed](#)]
41. Li, Y.; Dai, X.Y.; He, L.; Bu, Y.Y.; Ao, J.P. Crystal-reconstructed BiVO₄ semiconductor photoelectrochemical sensor for ultra-sensitive tumor biomarker detection. *J. Mater. Chem. B* **2022**, *10*, 870–879. [[CrossRef](#)] [[PubMed](#)]
42. Wu, Z.G.; Zhao, J.L.; Yin, Z.K.; Wang, X.L.; Li, Z.Q.; Wang, X.X. Highly sensitive photoelectrochemical detection of glucose based on BiOBr/TiO₂ nanotube array p-n heterojunction nanocomposites. *Sensor. Actuators B Chem.* **2020**, *312*, 127978. [[CrossRef](#)]
43. Liu, J.; Liu, Y.; Wang, W. Component reconstitution-driven photoelectrochemical sensor for sensitive detection of Cu²⁺ based on advanced CuS/CdS p-n junction. *Sci. China Chem.* **2019**, *62*, 1725–1731. [[CrossRef](#)]
44. Mazhabi, R.M.; Ge, L.Q.; Jiang, H.; Wang, X.M. A facile photoelectrochemical sensor for high sensitive ROS and AA detection based on graphitic carbon nitride nanosheets. *Biosens. Bioelectron.* **2018**, *107*, 54–61. [[CrossRef](#)]
45. Yang, L.W.; Li, L.; Li, F.; Zheng, H.J.; Li, T.T.; Liu, X.Q.; Zhu, J.C.; Zhou, Y.M.; Alwarappan, S. Ultrasensitive photoelectrochemical aptasensor for diclofenac sodium based on surface-modified TiO₂-FeVO₄ composite. *Anal. Bioanal. Chem.* **2021**, *413*, 193–203. [[CrossRef](#)]
46. Derikvand, H.; Roushani, M.; Abbasi, A.R.; Derikvand, Z.; Azadbakht, A. Design of folding-based impedimetric aptasensor for determination of the nonsteroidal anti-inflammatory drug. *Anal. Biochem.* **2016**, *513*, 77–86. [[CrossRef](#)]
47. Kashefi-Kheyrabadi, L.; Mehrgardi, M.A. Design and construction of a label free aptasensor for electrochemical detection of sodium diclofenac. *Biosens. Bioelectron.* **2012**, *33*, 184–189. [[CrossRef](#)]
48. Payan, M.R.; Lopez, M.A.B.; Fernandez-Torres, R.; Bernal, J.L.P.; Mochon, M.C. HPLC determination of ibuprofen, diclofenac and salicylic acid using hollow fiber-based liquid phase microextraction (HF-LPME). *Anal. Chim. Acta* **2009**, *653*, 184–190. [[CrossRef](#)]
49. Shi, T.Y.; Wen, Z.R.; Ding, L.J.; Liu, Q.; Guo, Y.S.; Ding, C.F.; Wang, K. Visible/near-infrared light response VOPc/carbon nitride nanocomposites: VOPc sensitizing carbon nitride to improve photo-to-current conversion efficiency for fabricating photoelectrochemical diclofenac aptasensor. *Sens. Actuators B Chem.* **2019**, *299*, 126834. [[CrossRef](#)]